Stereoscopic particle image velocimetry measurements of the flow around a Rushton turbine

D. F. Hill, K. V. Sharp, R. J. Adrian

Abstract The principles of stereoscopic particle image velocimetry (PIV), including distortion compensation, were applied to the turbulent flow in a vessel stirred by a Rushton turbine. An angular offset configuration was used and tilt-axis lens mounts were incorporated in order to satisfy the Scheimpflug condition, significantly reducing the ordinarily large depth of field requirements of such configurations. A distortion compensation procedure, or in situ calibration, was utilized in place of the ray tracing, or mechanical registration, used in previous studies. The calibration procedure was validated using two tests, one a rigid translation of a speckle target, the other the viscous flow between two concentric cylinders. The results of the tests suggest the success with which the distortion compensation procedure may be applied to real fluid flows. Phase-locked instantaneous data were ensemble averaged and interpolated in order to obtain mean 3-D velocity fields on a cylindrical shell enclosing the turbine blade. From these fields, the tip vortex pairs and the radial jet documented in previous studies of mixer flows were easily identified.

1
Introduction
Stereoscopic particle imaging techniques have broadly developed into two configurations: lateral offset and angular offset. Each method has its advantages and disadvantages, and significant progress has been made on each over the course of the past decade.

In the lateral offset configuration, the image planes, lens planes, and object plane are all parallel. As a consequence, perspective effects are minimized and the required depth of field is no greater than for conventional single-camera particle image velocimetry (PIV). However, a drawback

D. F. Hill
Department of Civil and Environmental Engineering
The Pennsylvania State University, 212 Sackett Building
University Park, PA 16802, USA

K. V. Sharp, R. J. Adrian
Department of Theoretical and Applied Mechanics
The University of Illinois at Urbana/Champaign
216 Talbot Laboratory, 104 S. Wright St.
Urbana, IL 61801, USA

Correspondence to: D. F. Hill

is the limited area in the flow field that is viewed by both cameras. Arroyo and Greated (1991), Prasad and Adrian (1993), and Liu et al. (1997) have all made important contributions to this stereoscopic imaging method.

In the angular offset configuration, on the other hand, the two cameras, rather than being displaced laterally, are rotated so that their image planes are no longer parallel to the object plane. The advantage of this configuration is the increased common field of view. Disadvantages, however, include the variable magnification that is introduced. Additionally, since the focal plane is no longer parallel to the object plane, a relatively small aperture is required to insure good focus over the entire field of view. Depending upon the laser power available and safety concerns, this may prove to be a serious constraint.

Grant et al. (1991) and Westerweel and Nieuwstadt (1991) both employed variations of the angular offset method. The former authors used a single camera and an arrangement of mirrors to produce the two stereoscopic views on the same piece of film. A calibration scheme was used to establish the relationship between the object plane and the image planes, but particle densities were so low as to render their work an application of particle tracking velocimetry (PTV) instead of PIV. The latter authors used CCD cameras to assess the performance of the angular offset method in the case of PIV. Rather than studying a real fluid flow, test images mounted on translation stages and computer-generated PIV images were used as the inputs to the interrogation and recombination algorithms.

More recently, Prasad and Jensen (1995) discussed a clever arrangement for an angular offset camera. Still based on ray tracing, their method involved satisfying the Scheimpflug condition through the use of a swing-back camera. Additionally, a liquid prism was utilized to minimize the radial distortions that are created by the air–liquid interface.

With the exception of Grant et al. (1991), all of the works discussed to this point have been based upon the mechanical registration of the film or CCD arrays. In other words, ray tracing had to be utilized to establish the mapping between the object plane and the image planes. A new, much more efficient alternative was recently put forth by Soloff et al. (1997). The general procedure outlined involved the acquisition of several images of a calibration target, say a cartesian grid of small dots, across the depth of the laser light sheet. These images were then used to, in a least squares sense, determine the magnification matrices

of the two cameras. This technique, which determines the mapping function between the image and object planes through mathematical registration, takes into account all the various distorting influences between the test section and the CCD arrays. This is advantageous, since even the most precise ray tracing will be subject to unknown errors due to slight misalignment of components.

Bjorkquist (1998) recently discussed the design of a stereoscopic system based on this compensation procedure. Incorporating tilt-axis Scheimpflug mounts to improve focusing, the author used the rigid translation of a test target to assess the performance of the calibration. The measured and known displacement fields were found to agree very well, though it should be noted that the tests were carried out in the absence of any significant distortion.

The goal of the current work, therefore, is to apply the principles of stereoscopic PIV, with distortion compensation, to a real fluid flow. The turbulent flow around a Rushton turbine was chosen both because it has been an area of ongoing research in the Laboratory for Turbulence and Complex Flow at the University of Illinois and because, possessing strong radial and circumferential velocity components, it is an ideal testing ground for the procedure.

The calibration procedure is first validated in two ways. First, the rigid translation of a test target in the presence of realistic optical distortion is investigated. Secondly, the viscous flow of glycerin between concentric cylinders is investigated and the measured velocities are compared with the exact solutions. In both instances, the calibration is found to perform well.

Phase-locked data are then obtained on a variety of planes and at a variety of rotational speeds. By ensemble averaging and then interpolating the data, mean 3-D velocity fields are obtained on a cylindrical surface enclosing the turbine blade.

2
Experimental apparatus and procedure

2.1
Overview of apparatus

A schematic overhead view of the experimental set-up and data acquisition system is shown in Fig. 1. While not strictly to scale, the figure does reflect fairly well the fact that the object-to-lens distance was roughly three times the image-to-lens distance. The Rushton turbine had a diameter (D) of 50.8 mm, a blade height (H) of 10 mm, and was connected via a 9.52-mm-diameter stainless-steel shaft to a Lightnin mixer (Model no. L1U08F).

The cylindrical mixing tank was unbaffled and had an inner diameter given by $T = 3D = 15.24$ cm. The tank was filled to a depth T with de-ionized water and the turbine blade was centered vertically on the centerline of the tank. To reduce the optical distortion of the curved surface of the test section, the cylinder was placed in a square acrylic container of inner dimension 21 cm, which was also filled with de-ionized water. It should be noted that further reductions in the distortion caused by the optical interfaces could have been achieved by matching the index of refraction of the working fluid to that of the acrylic walls. However, this was not pursued, since the goal of the study
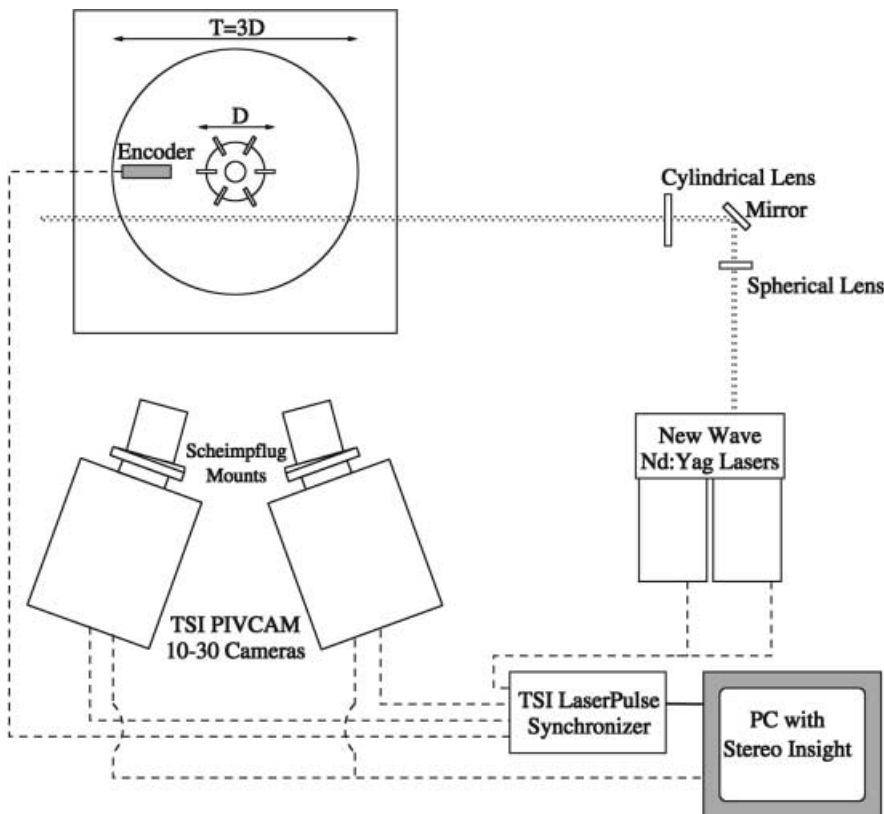

Fig. 1. Overhead schematic of experimental apparatus and data acquisition system

was to overcome sources of distortion that are commonly encountered in the laboratory.

The flow was illuminated with two New Wave Nd:Yag pulsed lasers, operating nominally at 12 mJ/pulse. A spherical lens, high-energy mirror and cylindrical lens were used to create a light sheet 1 mm thick and ~4 cm high in the test section. The flow was seeded with 8 μm polystyrene particles.

Two TSI PIVCAM 10-30 CCD cameras (Model no. 640046, 1 K by 1 K resolution) were used to acquire images of the flow. The cameras were equipped with Nikon AF Micro Nikkor 60-mm lenses and were positioned such that there was an included angle of ~40° between them. To reduce the required depth of field, tilt-axis mounts were installed between the camera bodies and lenses and were adjusted in order to satisfy the Scheimpflug condition. The configuration of the mounts was such that the camera body was held fixed while the lenses rotated. While the precise angle of tilt required could have been calculated theoretically, the mounts lacked a precise scale for reading the tilt. As such, an iterative process of adjusting the tilt and repositioning the camera slightly was pursued until good focus was achieved over the entire field of view. In the end, tilt angles on the order of 5° were sufficient. It should be noted that currently available Scheimpflug lens mounts rotate the camera while holding the lens fixed, which will alleviate this iterative procedure.

The cameras and lasers were connected to a PC via a TSI Laser Pulse synchronizer, which controlled the timing of the data acquisition. An encoder mounted on the test section and focused on the mixer shaft triggered the acquisition and enabled phase-locked data to be obtained. Finally, the images were acquired using TSI's Stereo Insight software.

2.2
Calibration procedure

Due to the substantial optical distortion resulting from the off-axis alignment of the cameras and the refractive properties of the water and acrylic, it was necessary to calibrate the cameras every time a new plane of acquisition was chosen. As discussed in the introduction, the mechanical registration of the CCD arrays used in previous studies has here been replaced by a mathematical registration. This distortion compensation procedure is detailed by Soloff et al. (1997) and is only briefly summarized here.

The optical distortion cited above results in variable magnification across the field of view of the cameras. The relationships between points in the object plane and points in the image planes can no longer be described by simple geometric constructs. The general procedure of the calibration, therefore, is to determine these relationships in an in situ manner. A series of images of a calibration target, say a regular cartesian grid of small circular marks, is acquired across the depth of the light sheet. A mapping function is then determined from the known locations of the marks in the object plane and the apparent locations of the marks in the image planes. With this mapping function determined, stereoscopic displacement fields obtained

during the experiment are readily recombined into 3-D velocity vector fields.

To accomplish this in the current experiment, a target consisting of 400-μm diameter white dots on a black anodized aluminum surface was used. The dots were spaced at intervals of 2.5 mm and the target was of sufficient size to entirely fill the fields of view of the cameras. The front surface of the target was aligned with the center of the light sheet, and then calibration images were obtained at five locations across the depth of the light sheet. The spacing between these images was 250 μm so that the entire thickness of the light sheet was included in the calibration region.

Finally, with the calibration images acquired, the mapping function was determined. The function was taken to be a multi-dimensional polynomial and was obtained using the method of least squares. The polynomial was chosen to be cubic in the in-plane coordinates and quartic in the out-of-plane coordinate. Once the polynomial coefficients had been determined, the rms error in the mapping function could be computed for each component and for each camera. An average of these individual rms errors for a given camera yielded a representative measure of the accuracy of the calibration for that camera. For one set of experiments carried out in this paper, the average rms error in the mapping function for the left camera was 0.18 pixels and the average rms error for the right camera was 0.21 pixels.

Once the mapping function had been established, some test images were used to investigate the degree of variability of magnification across the image planes. As discussed by Soloff et al. (1997), the usual concept of magnification, in the presence of distortion, is generalized to a matrix defined by the gradients of the mapping function, $\mathbf{F}(\mathbf{x}) = \mathbf{X}$, that maps the object space $\mathbf{x}$ to the image space $\mathbf{X}$.

$$(\nabla F)_{ij} = \frac{\partial F_i}{\partial x_j} = F_{i,j} \quad i = 1, 2 \quad j = 1, 2, 3$$

The relationship between the object and image displacements is then given by

$$\Delta X_i \simeq F_{i,j} \Delta x_j \ .$$

For a stereoscopic system, where two cameras are present, the mapping at any point is therefore given by

$$\begin{bmatrix} \Delta X_1^L \\ \Delta X_2^L \\ \Delta X_1^R \\ \Delta X_2^R \end{bmatrix} = \begin{bmatrix} F_{1,1}^L & F_{1,2}^L & F_{1,3}^L \\ F_{2,1}^L & F_{2,2}^L & F_{2,3}^L \\ F_{1,1}^R & F_{1,2}^R & F_{1,3}^R \\ F_{2,1}^R & F_{2,2}^R & F_{2,3}^R \end{bmatrix} \begin{bmatrix} \Delta x_1 \\ \Delta x_2 \\ \Delta x_3 \end{bmatrix} \ . \tag{1}$$

The easiest way to compute the terms in the magnification matrix is to move an artificial image target a known displacement in a single direction, say the x_1 direction, compute the image displacements, and use Eq. (1) to compute the appropriate terms of the matrix. In the case of a pure x_1 object displacement, the first column of the magnification matrix is immediately determined. This procedure was carried out for both x_1 displacements and x_3 displacements. The first and third columns of the magnification matrices at the extreme corners of the object plane were computed and are given, in pixels/mm, by

$$\begin{bmatrix} 30.3 & F_{1,2}^L & \mathbf{5.59} \\ -0.177 & F_{2,2}^L & 0.598 \\ 29.1 & F_{1,2}^R & \mathbf{-6.91} \\ 0.366 & F_{2,2}^R & 0.440 \end{bmatrix} \quad \begin{bmatrix} 29.1 & F_{1,2}^L & 6.52 \\ -0.147 & F_{2,2}^L & 0.499 \\ 30.5 & F_{1,2}^R & -6.20 \\ 0.391 & F_{2,2}^R & 0.512 \end{bmatrix}$$

$$\begin{bmatrix} 30.2 & F_{1,2}^L & 5.79 \\ 0.546 & F_{2,2}^L & -1.10 \\ 29.1 & F_{1,2}^R & -6.67 \\ -0.364 & F_{2,2}^R & -1.21 \end{bmatrix} \quad \begin{bmatrix} 29.4 & F_{1,2}^L & 6.37 \\ 4.05 & F_{2,2}^L & -0.873 \\ 30.3 & F_{1,2}^R & -6.09 \\ -0.403 & F_{2,2}^R & -1.23 \end{bmatrix}$$

A great deal of insight can be gained from a quick inspection of the relative magnitudes, as well as signs, of the components of the magnification matrices. As an example, the two bold values are measures of the horizontal image displacements resulting from a pure x_3 object displacement, as seen by the left and right cameras, respectively. As indicated by the change in sign, the two cameras see the pure out-of-plane object displacement as image displacements in opposite directions.

2.3
Acquisition of data
As indicated in Fig. 2, data were obtained in three $x–y$ planes. Note that, hereafter, the coordinates (x, y, z) are used in place of (x_1, x_2, x_3). The planes were displaced from the centerline of the tank by distances of 22.94, 25.44 and 26.94 mm. The resulting nominal in-plane magnifications were 0.278, 0.281 and 0.283. The trigger delay was adjusted such that the blades were in the position shown at the time of acquisition. It is important to note that the encoder triggered the synchronizer only once per revolution, so that all the acquired images were of the same sextant of the turbine.

Experimental runs were carried out for rotational rates (ω) of 50, 100 and 150 rpm. In each case, and for each location, one hundred realizations were obtained.

2.4
Data processing
The first step in processing the data was to interrogate and validate separately the image pairs from the left camera and the images pairs from the right camera. This was done using two software packages, PIVSleuth (Christensen and Soloff 1998, private communication) and Cleanvec (Meinhart and Soloff 1997, private communication), both developed in the Laboratory for Turbulence and Complex Flow.

In the interrogation, the first and second windows were taken to be 32 × 32 and 64 × 64 pixels, respectively, the FFT window size was set to 64 × 64, and a 50% overlap was used. The resulting grid resolutions for the three planes were therefore 1.13, 1.14 and 1.15 mm, respectively. During the validation for the two planes furthest from the tank axis, typically very few, if any, vectors were removed. For the plane closest to the tank axis, typically 1% of the vectors were removed. These bad vectors were due to reflections from the blade tips which saturated portions of the CCD arrays. Finally, the validated fields from the left and right cameras were recombined in the manner discussed above. Note that in this last step, the recombined velocity vectors can be computed directly onto a user-defined grid. This flexibility is a benefit of the mapping procedure and its advantages will become apparent in the discussion of the results.

3
Results
Before beginning the data acquisition, it was desired to evaluate the success of the calibration procedure in compensating for the significant distortion in the set-up. To this end, two tests were carried out: one the rigid translation of a computer-generated speckle target, the other the viscous flow between two concentric cylinders.

3.1
Rigid body translation
In the first test, the speckle target was placed in the test section after the completion of the calibration. Translation stages moved the target in various combinations of directions, simulating the motion of seed particles in fluid. Three cases were considered, pure x motion, pure z motion, and combined x and z motion. In all cases, the displacement in each direction of motion was 0.5 mm.
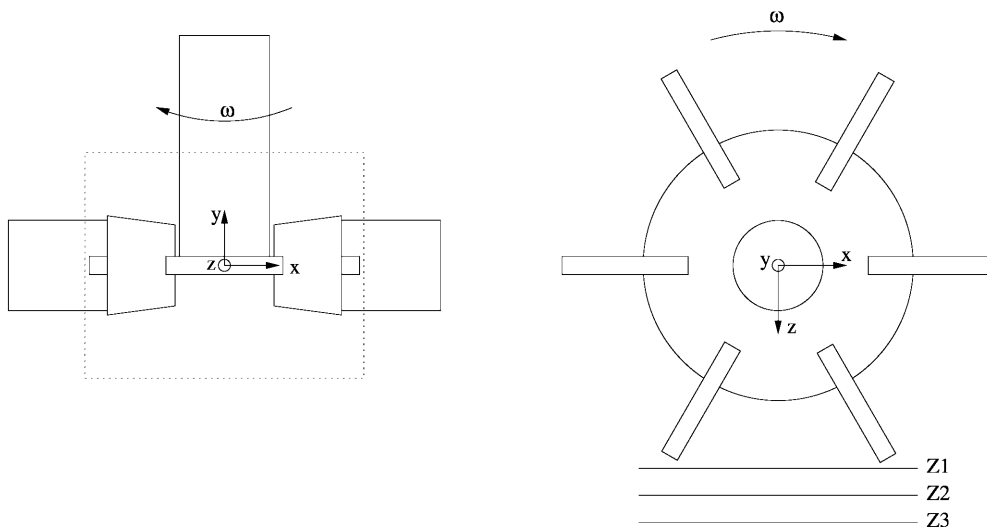
481

Fig. 2. Side and top views of the data acquisition planes

Table 1. Comparison between the known and measured rigid-body translations of a test speckle target

Translation (μm)	$\langle \Delta x \rangle_A$	$\langle \Delta y \rangle_A$	$\langle \Delta z \rangle_A$	$\sigma_{\Delta x}$	$\sigma_{\Delta y}$	$\sigma_{\Delta z}$
$-\Delta z = 500$	-2.04	0.0771	490	0.0187	0.0415	0.142
$-\Delta x = -500$	-490	0.0834	23.6	0.0726	0.121	0.129
$-\Delta x = \Delta z = 500$	-490	0.0982	523	0.0563	0.143	0.167

For each case, ten realizations were measured. After processing, the ten 3-D displacement fields were ensemble averaged to obtain a mean displacement field, $\langle \underline{\Delta x}(x, y) \rangle$. The area-average of this mean field, $\langle \underline{\Delta x} \rangle_A$, was then computed as were the rms values of the estimate of the mean. The results are summarized in Table 1.

Clearly, the stereoscopic calibration performed well. The measured in-plane motion $\langle \Delta x \rangle_A$ was found to agree with the known in-plane motion to within 2%. In the case of out-of-plane motion only, $\langle \Delta z \rangle_A$ was found to agree with the known out-of-plane motion to within 2%, while in the case of simultaneous in-plane and out-of-plane motion, $\langle \Delta z \rangle_A$ agreed with the known displacement to within 5%.

3.2
Cylindrical Couette flow
While useful, the rigid translation of artificial particle images was not a fully realistic test procedure, because displacement gradients were negligible and the particle images were, after all, artificial. Indeed, one wishes to retain as many characteristics of the actual experiment as possible when performing a validation. Therefore, as a second test, the calibration procedure was validated against a real fluid flow with velocity gradients.

Given the geometry of the test section, the flow between two concentric cylinders was a natural candidate. The turbine was removed from the test section and was replaced by a 9.52-mm-diameter stainless-steel shaft, which extended to the bottom of the tank. Glycerin was used as the working fluid, and the flow was seeded with the same particles used in the mixing experiments.

The shaft was rotated at 150 rpm so that the analytical expression for the circumferential velocity was given by $u_\theta(r) = -4.69(76.3/r - r/76.3)$ mm/s. Images were acquired at a plane centered vertically and displaced 25 mm radially from the centerline of the tank. After completing the calibration, 100 realizations were obtained.

After processing and recombination, the vector fields were ensemble averaged. This mean field was then transformed from a cartesian to a polar coordinate system. Finally, the ensemble-averaged vectors were averaged along vertical lines, yielding $\langle u_\theta(r) \rangle_y$.

These measured values, along with the theoretical predictions, are presented in Fig. 3. The error bars indicate $\pm 2\sigma$, where σ is the rms value of the estimate of the mean. It should be noted that one possible source of error in this test may be that the shaft was observed to wobble slightly from side to side in a periodic fashion. Despite the relative precision of the LabMaster mixer, the motion is not perfect. As indicated in the figure, however, the agreement
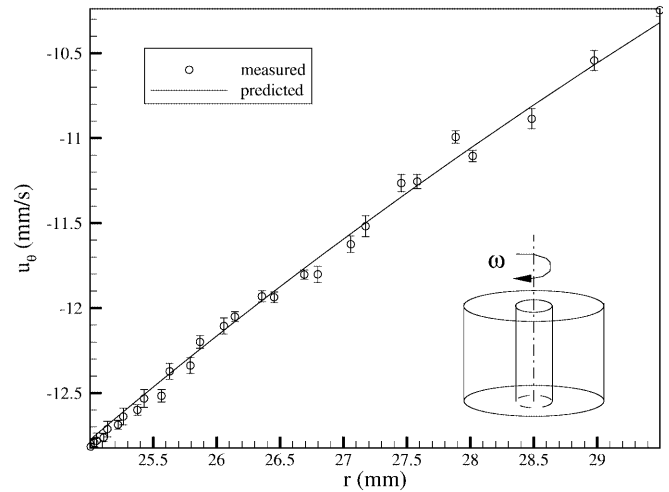

Fig. 3. Comparison between measured and predicted U_θ for the flow of glycerin between two cylinders. The inset sketch indicates the direction of rotation of the inner cylinder. Error bars indicate $\pm 2\sigma$, where σ is the rms value of the estimate of the mean

between the data and analytical prediction is quite good. This was considered to be a successful validation of the distortion compensation procedure.

3.3
Three-dimensional velocity results
A sample instantaneous velocity field in the plane of acquisition furthest from the tank centerline is shown in Fig. 4. The vectors represent the in-plane velocities u and v, while the contours denote the out-of-plane velocity w. All of the velocity components have been scaled by the blade tip velocity, U_{tip}, whose magnitude is shown as a reference vector. For clarity, every other vector in both directions was omitted, so that only 25% of the vectors are shown.

With regards to the out-of-plane motion, note that, in general, the right half of the contour plot shows positive w, while the left half of the plot shows negative values of w. This is clearly due to the mean circumferential velocity driven by the rotating blades. The highly concentrated region of positive w sandwiched between similar regions of negative w in the left half of the plot indicates the presence of the shed blade vortex pair. These vortices are also identifiable in the vector fields, indicating that they are oblique to the acquisition planes.

To aid in the physical interpretation of the data and to make it more suitable for incorporation as boundary conditions to numerical models, the data were ensemble averaged and then interpolated onto a cylindrical surface. This was achieved in several steps.

First, when the stereoscopic velocity vector fields were recombined, the grids on the three acquisition planes were chosen so that they lined up on radial lines. Recall that the recombination procedure was designed with this flexibility in mind. Next, the instantaneous fields were ensemble averaged to yield a mean velocity field, $\langle \underline{u}(x, y) \rangle$ for each plane. These mean fields were then interpolated, using a second-order fit, onto the curved surface given by $r = 26.5$ mm, as shown in Fig. 5. Finally, the cartesian
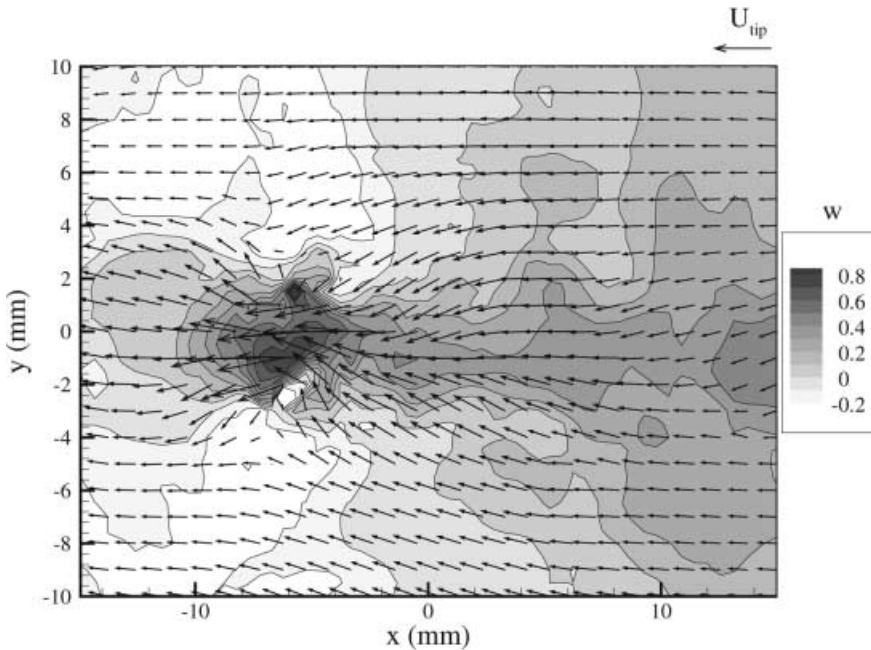
Fig. 4. Sample instantaneous 3-D velocity field at the $z = 26.95$ mm acquisition plane. The contours indicate the out-of-plane component of velocity. All velocity components have been normalized by the blade tip velocity. $\omega = 100$ rpm. Every other vector in both directions has been omitted for clarity
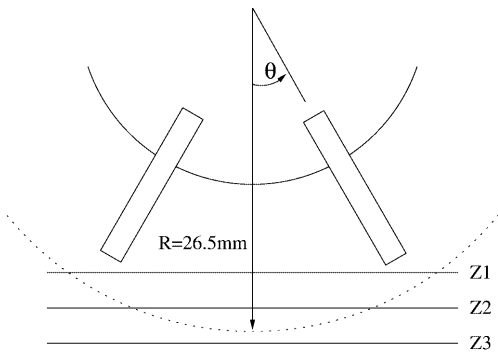

Fig. 5. Schematic showing relationship between the acquisition planes and the cylindrical surface onto which the data were interpolated

velocity components were transformed into polar velocity coordinates, yielding $\langle \underline{u}(y, \theta) \rangle$, where $u = (u_r, u_\theta, u_y)$.

The fields of view of the cameras during the experiments were sufficiently large that data on an arc subtending an angle of 60° could be obtained in this manner. Given the 60° periodicity of the Rushton turbine, data were therefore essentially obtained on a cylindrical surface enclosing the whole turbine.

A variety of views of the ensemble-averaged and interpolated velocity data for the 100 rpm case is shown in Fig. 6. In this case, the vectors represent circumferential and axial velocity, while the contours denote radial velocity. In each plot, the velocity components have been scaled by U_{tip} and the vertical coordinate has been scaled by the blade height. Figure 6a shows all three components of the velocity, while Fig. 6b contains horizontal slices showing only the radial and circumferential components, and Fig. 6c contains vertical slices detailing the radial and axial components. As indicated in the figure caption, vectors have been omitted in Fig. 6a and b for the sake of clarity of presentation.

The presence of the vortices in Fig. 6a is very clear, as is a strong radial jet and a background circumferential flow. The jet is well documented and is part of the tank-scale circulation set up in mixing vessels. The slices in Fig. 6b clearly demonstrate that the radial velocity of the jet is a fairly weak function of θ, except in the vicinity of the vortex pair, where, depending upon y/H, the jet flow is either reinforced or reversed. The one vector in Fig. 6b which appears to be an error is actually due to the blade reflections mentioned in Sect. 2.4. Due to these reflections, there were a few grid points in the closest acquisition plane for which no acceptable data were obtained. As a result, the quadratic interpolation mentioned above was reduced to a linear extrapolation at these few points, clearly with poor results. These problematic points can also be seen at the extreme right of Fig. 6a, where the velocity is erroneously large.

The reversal of flow induced by the vortices is also visible in the vertical slices shown in Fig. 6c. There is a strong core of positive radial velocity, between two regions of negative radial velocity, located at $\theta = 20°$. With increasing θ, the contribution of the vortex pair to the velocity components quickly decays. This is because the radial position of the vortex pair is an increasing function of degrees since blade passage.

As a final note on the ensemble-averaged data, both the radial and circumferential velocities achieve maximum values on the order of the tip velocity. This fact that $u_r \sim O(u_\theta)$ highlights the need for stereoscopic measurements of the flow around a Rushton turbine. In conventional single-camera PIV, there is a perspective error introduced by out-of-plane motion. This error is proportional to the ratio of out-of-plane to in-plane displacement. As an estimate of this error, consider a 30 mm field of view situated at an object distance of 300 mm. If the in-plane and out-of-plane displacements are of a similar magnitude, the maximum error between real and apparent in-plane motion will be ~5% and will occur near the

484

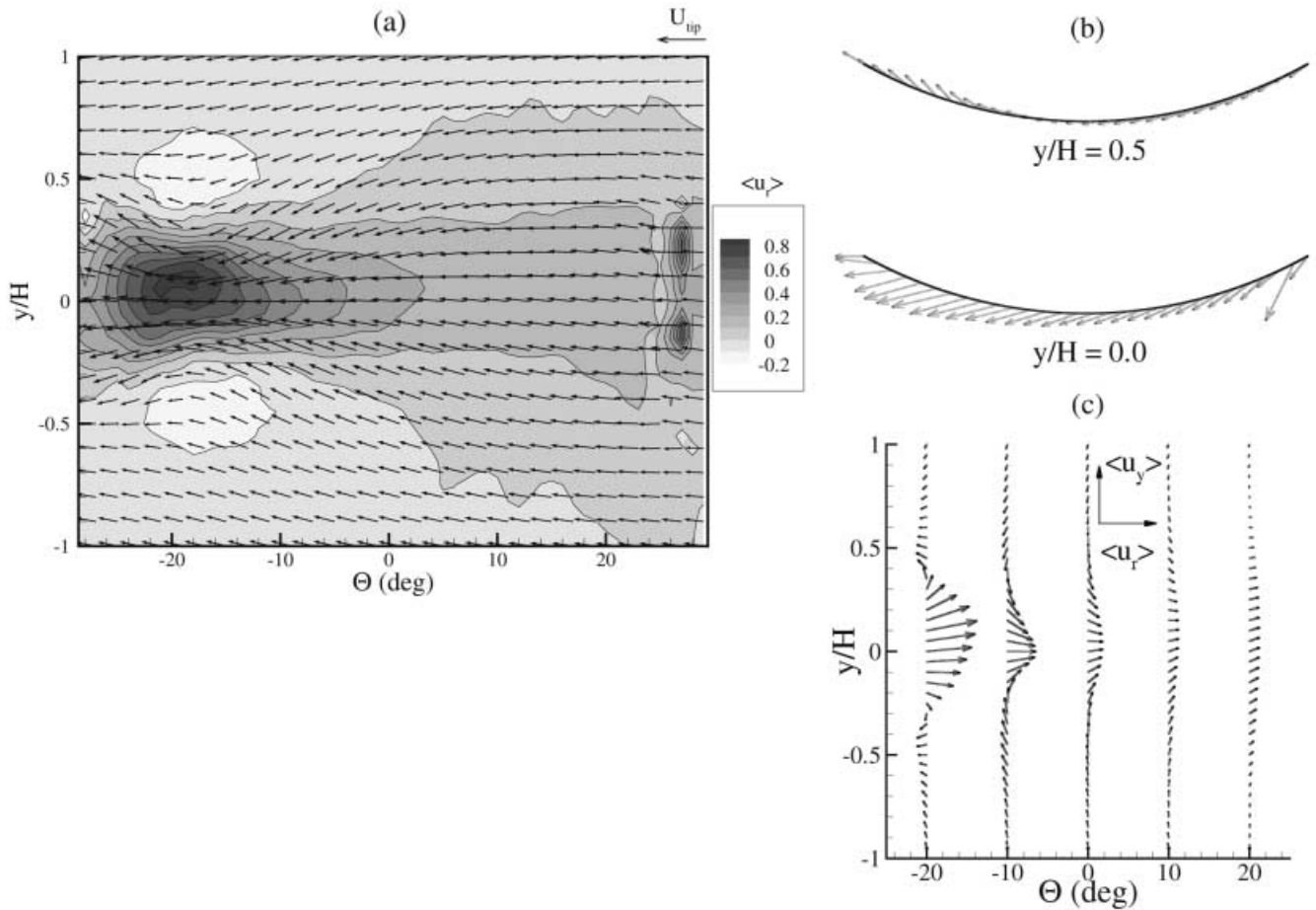**Fig. 6. a** Mean 3-D velocity fields interpolated on $R = 26.5$ mm surface. Every other vector in both directions has been omitted for clarity. **b** Horizontal slices showing radial and circumferential

components. Every other vector in the θ direction has been omitted for clarity. **c** Vertical slices showing radial and axial components

perimeter of the field of view. Previous 2-D PIV studies of the flow in mixing tanks (Sharp et al. 1998; Sheng et al. 1998) have sought to measure radial and axial velocity, with circumferential velocity being the unrealizable out-of-plane component. As such, their measurements were subject to this perspective error, while the current measurements are not.

The velocity fields presented to this point have been in the lab frame of reference. Due to the large circumferential component of velocity, however, the vortices are perhaps not as readily apparent as might be expected. Adrian et al. (1998) have recently discussed this issue of vortex identification, the success of which is crucially dependent upon proper reference frame selection. A natural alternative in this case is to consider the data in the blade frame of reference by subtracting the tip velocity from $\langle u_\theta(y, \theta) \rangle$. A second alternative is to subtract $\langle u_\theta \rangle_A$, the area-averaged circumferential velocity from $\langle u_\theta(y, \theta) \rangle$.

The ensemble-averaged data from the 100-rpm experiment are shown in these three frames of reference in Fig. 7. From the first two plots, it is clear that the vortices have a convective velocity significantly less than the tip velocity. The high shear in the vicinity of the blades results in the vortices being quickly left behind by the blade tips. The final choice of reference frame is clearly the most

successful, offering a very clear snapshot of the vortices, including their locations and diameters.

4
Concluding remarks

The principles of stereoscopic PIV were applied to the flow around a Rushton turbine. This marks the first full implementation and application of the procedure detailed by Soloff et al. (1997) to a real fluid flow. The chosen flow field and accompanying experimental configuration were a suitable testing ground for the procedure due to the strong three-dimensionality of the flow and the significant optical distortion present.

The chief advantage of the mathematical registration used in this work is that it does not require the time-consuming precision that mechanical registration does when it comes to setting up the system. Additionally, it takes into account all the distorting influences between object plane and image plane, including those, such as a slightly misaligned CCD chip which ray tracing cannot.

The compensation procedure was validated using two tests, both of which included optical distortion and the latter of which was a real fluid flow possessing velocity gradients. Velocity data around the turbine were then collected, ensemble averaged, and interpolated in order to
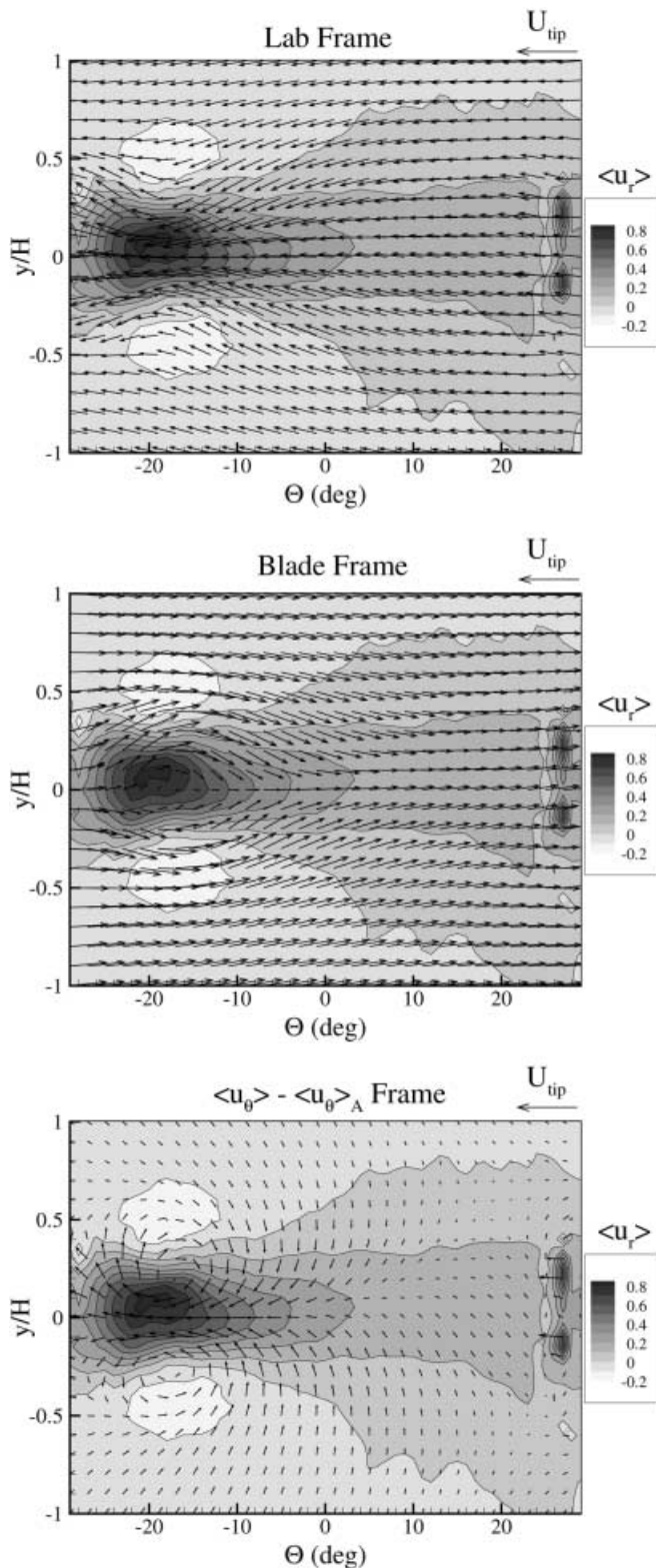
Fig. 7. Mean 3-D velocity fields in three different reference frames. Data have been interpolated onto $R = 26.5$ mm surface and $\omega = 100$ rpm. Every other vector in both directions has been omitted for clarity

obtain the mean velocity field on a cylindrical surface enclosing the turbine. The radial jet and blade tip vortices which are responsible for driving the large-scale circulation in the tank were easily identified from these data. Finally, measurements revealed that, in the near-blade region, the radial and circumferential velocity components were of equal order, highlighting the need for detailed stereoscopic measurements of this complex flow.

References

Adrian RJ; Christensen KT; Soloff SM; Meinhart CD; Liu Z-C (1998) Decomposition of turbulent fields and visualization of vortices. In: Proc Ninth Int Symp on Applications of Laser Techniques to Fluid Mechanics, pp 16.1.1–16.1.8

Adrian RJ; Christensen KT; Liu Z-C (2000) Analysis and interpretation of instantaneous velocity fields. Experiments in Fluids, in press

Arroyo MP; Greated CA (1991) Stereoscopic particle image velocimetry. Meas Sci Tech, vol. 2. pp 1181–1186

Bjorkquist D (1998) Design and calibration of a stereoscopic particle image velocimetry system. In: Proc Ninth Int Symp on Applications of Laser Techniques to Fluid Mechanics, pp 6.5.1–6.5.8

Additional information is that the conference was held in Lisbon, Portugal on July 13–16, 1998

Grant I; Zhao Y; Tan Y; Stewart JN (1991) Three component flow mapping: experiences in stereoscopic particle image velocimetry and holographic velocimetry. In: Dybbs A, Ghorashi B (eds) Laser anemometry advances and applications, vol. 1. ASME, New York, pp 349–355

Liu Z-C; Adrian RJ; Meinhart CD; Lai W (1997) Structure of a turbulent boundary layer using a stereoscopic, large-format video-PIV. In: Adrian RJ, Durao DFG, Durst F, Heitor MV, Maeda M, Whitelaw JH (eds) Developments in laser techniques and fluid mechanics. Springer, New York Berlin Heidelberg, pp 259–273

Prasad AK; Adrian RJ (1993) Stereoscopic particle image velocimetry applied to liquid flows. Exp Fluids 15: 49–60

Prasad AK; Jensen K (1995) Scheimpflug stereocamera for particle image velocimetry in liquid flows. Appl Optics 34: 7092–7099

Sharp K; Kim KC; Adrian RJ (1998) Dissipation estimation around a Rushton turbine using particle image velocimetry. In: Proc Ninth Int Symp on Applications of Laser Techniques to Fluid Mechanics, pp 14.1.1–14.1.10

Sharp KV; Kim KC; Adrian RJ (2000) Dissipation estimation around a Rushton turbine using particle image velocimetry, "Laser Techniques Applied to Fluid Mechanics: Selected Papers from the 9th Intl. Symp., Edited by Adrian RJ, Durao DFG. Lisbon, Portugal, July 13–16, 1998

Sheng J; Meng H; Fox RO (1998) Validation of CFD simulations of a stirred tank using particle image velocimetry data. Can J Chem Eng 76: 611–625

Soloff SM; Adrian RJ; Liu Z-C (1997) Distortion compensation for generalized stereoscopic particle image velocimetry. Meas Sci Technol 8: 1441–1454

Westerweel J; Nieuwstadt FTM (1991) Performance tests on 3-dimensional velocity measurements with a two-camera digital particle image velocimeter. In: Dybbs A, Ghorashi B (eds) Laser anemometry advances and applications, vol. 1. ASME, New York, pp 349–355